

# A Thesis Title

*Author Name*

A dissertation submitted in partial fulfillment  
of the requirements for the degree of  
**Doctor of Philosophy**  
of  
**University College London.**

Department of Something  
University College London

August 3, 2017

I, Author Name, confirm that the work presented in this thesis is my own. Where information has been derived from other sources, I confirm that this has been indicated in the work.

# **Abstract**

My research is about stuff.

It begins with a study of some stuff, and then some other stuff and things.

There is a 300-word limit on your abstract.

# Acknowledgements

Acknowledge all the things!

# Contents

<b>1</b>	<b>Introductory Material</b>	<b>10</b>
<b>2</b>	<b>The ATLAS Detector</b>	<b>11</b>
2.1	The Large Hadron Collider . . . . .	11
2.1.1	LHC running conditions in 2015 and 2016 . . . . .	11
2.2	ATLAS Detector Description . . . . .	12
2.2.1	ATLAS Co-ordinate System . . . . .	12
2.2.2	Inner Detector . . . . .	15
2.2.3	Calorimeters . . . . .	17
2.2.4	Muon Spectrometer . . . . .	20
2.2.5	Magnets . . . . .	21
2.3	Trigger . . . . .	21
<b>3</b>	<b>Triggering in the di-<math>b</math>-jet analysis</b>	<b>24</b>
3.1	Jet-Triggers . . . . .	24
3.1.1	Level 1 . . . . .	24
3.1.2	HLT . . . . .	25
3.1.3	High-mass trigger selection . . . . .	25
3.2	$b$ -Jet Triggers . . . . .	26
3.2.1	General description . . . . .	26
3.3	Efficiency Measurement of the $b$ -Jet Trigger . . . . .	27
3.3.1	Strategy . . . . .	28
3.3.2	Datasets . . . . .	29
3.3.3	Event Selection . . . . .	29
3.3.4	The Initial Problem . . . . .	30

<i>Contents</i>	<i>6</i>
3.3.5 Investigation and Solution . . . . .	31
3.3.6 Measurement and Systematic Assignment . . . . .	34
3.3.7 Cross-checks . . . . .	34
<b>4 General Conclusions</b>	<b>35</b>
<b>Appendices</b>	<b>36</b>
<b>A An Appendix About Stuff</b>	<b>36</b>
<b>B Another Appendix About Things</b>	<b>37</b>
<b>C Colophon</b>	<b>38</b>
<b>Bibliography</b>	<b>39</b>

# List of Figures

2.1	Cumulative luminosity versus time delivered to (green) and recorded by ATLAS (yellow) during stable beams for pp collisions at 13 TeV centre-of-mass energy in (a) 2015 and (b) 2016. . . . .	12
2.2	A cut-away schematic of the ATLAS detector. . . . .	13
2.3	A visualisation of the ATLAS detector and the various sub-detectors. The view is taken as a slice in a plane perpendicular to the beam-pipe, showing the radial range from the beam-pipe to the edge of the detector. Overlaid are simplified illustrations of how various types of particles interact with the ATLAS detector; specifically from left to right the particles are an electron, a chargeless hadron (e.g. a neutron), a photon, a muon and a charged hadron (e.g. proton). The sub-detector components are not to scale. . . . .	14
2.4	A cut-away schematic of the ATLAS Inner Detector (ID). . . . .	16
2.5	A cut-away schematic of the ATLAS calorimeter system. . . . .	18
2.6	The layout of the ATLAS magnets. . . . .	22
2.7	A schematic of the ATLAS trigger and data-acquisition system in Run-2, with a focus on the components required for triggering. . . . .	23
3.1	The expected $b$ -jet efficiency of $b$ -jet triggers with respect to (a) light-jet and (b) $c$ -jet rejection in the case where the $b$ -tagging algorithm used is MV2c20 (Black), IP3D+SV1 (Blue) and for the set-up used in Run-1 (red stars). . . . .	27
3.2	The 60% $b$ -jet trigger efficiency with respect to an offline 70% operating point tag for data from Data (black) and simulation (red) against jet- $p_T$ (left), jet- $\eta$ (right). The $b$ -trigger aware GRL is not applied and trigger matching is not required. . . . .	30

- 3.3 The 60%  $b$ -jet trigger efficiency with respect to an offline 70% operating point tag for data from Epoch 1 (black) and simulation (red) against jet- $p_T$  (upper left), jet- $\eta$  (upper right), vertex class (lower left) and online beamspot z-position (lower right). . . . . 32
- 3.4  $b$ -perf efficiency,  $\varepsilon_{bPerf}$ , for data from Epoch 2 (black) and simulation (red) against leading-jet  $p_T$  (left) and online beamspot z-position (right). . . . . 33
- 3.5 The 60%  $b$ -jet trigger efficiency with respect to an offline 70% operating point tag for data from epoch 2 (black) and simulation (red) against jet- $p_T$  (left), jet- $\eta$  (right) and online beamspot z-position (lower). . . . . 33
- 3.6 The 60%  $b$ -jet trigger efficiency with respect to an offline 70% operating point tag for data from Epoch 3 (black) and simulation (red) against jet- $p_T$  (upper left), jet- $\eta$  (upper right) and vertex class (lower. . . . . 34



# List of Tables

3.1	A table describing the effect of not finding a valid xPrmVtx primary vertex on different epochs of data. . . . .	31
-----	---	----

## Chapter 1

# Introductory Material

Some stuff about things.[?] Some more things.

Inline citation:

Lorem ipsum dolor sit amet, consectetur adipiscing elit. Etiam lobortis facilisis sem. Nullam nec mi et neque pharetra sollicitudin. Praesent imperdiet mi nec ante. Donec ullamcorper, felis non sodales commodo, lectus velit ultrices augue, a dignissim nibh lectus placerat pede. Vivamus nunc nunc, molestie ut, ultricies vel, semper in, velit. Ut porttitor. Praesent in sapien. Lorem ipsum dolor sit amet, consectetur adipiscing elit. Duis fringilla tristique neque. Sed interdum libero ut metus. Pellentesque placerat. Nam rutrum augue a leo. Morbi sed elit sit amet ante lobortis sollicitudin. Praesent blandit blandit mauris. Praesent lectus tellus, aliquet aliquam, luctus a, egestas a, turpis. Mauris lacinia lorem sit amet ipsum. Nunc quis urna dictum turpis accumsan semper.

## Chapter 2

# The ATLAS Detector

### 2.1 The Large Hadron Collider

High-energy particle colliders have been an essential tool in high-energy physics research for over 50 years, with a rich history of discovering new particles as each generation of collider pushes the energy frontier; including the discovery of the Z and W bosons using the Super Proton Synchrotron at CERN in 1983 [1, 2, 3, 4] and the discovery of the top-quark at the Tevatron in 1995 [5, 6].

The Large Hadron Collider (LHC) is the highest energy collider ever built, operated by the *Conseil Européen pour la Recherche Nucléaire (CERN)*. Lying in a tunnel 100 m beneath the Swiss/French border near Geneva, the LHC is a 27 km circumference ring of superconducting magnets and accelerating structures, which accelerate beams of protons to a maximum energy of 6.5 TeV. These proton beams are collided in four different locations on the LHC ring and around each collision point a different detector is constructed to observe these collisions; one such of these detectors is ATLAS.

#### 2.1.1 LHC running conditions in 2015 and 2016

Since May 2015 the LHC has been colliding bunches of protons at a center-of-mass energy of 13 TeV, the highest energy collisions ever obtained by a particle collider <sup>1</sup>. In 2015 and 2016 the LHC produced pp collisions with a bunch spacing of 25 ns<sup>2</sup> and an average number of collisions per bunch-crossing ( $\langle \mu \rangle$ ) of 23.7. Figure 2.1 shows the total luminosity delivered by the LHC and recorded by ATLAS against date in 2015 and 2016, showing that

---

<sup>1</sup>The period of data-taking from 2015 is known as Run-2.

<sup>2</sup>A small amount of data in 2015 was collected with a bunch spacing of 50 ns

a luminosity of  $39.5 \text{ fb}^{-1}$  was recorded by ATLAS in 2015 and 2016 combined [7].

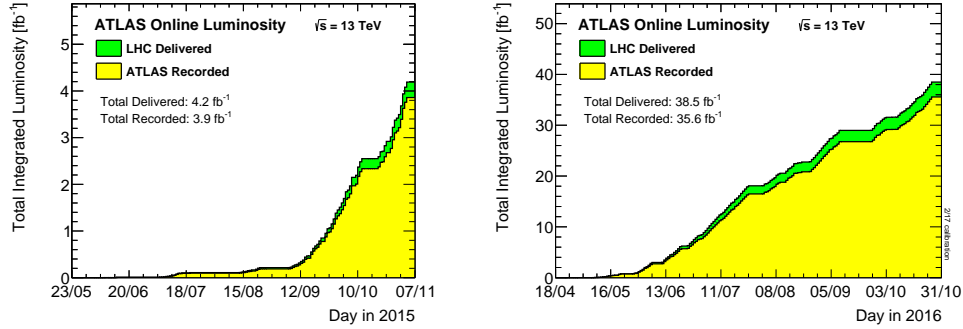


**Figure 2.1:** Cumulative luminosity versus time delivered to (green) and recorded by ATLAS (yellow) during stable beams for pp collisions at 13 TeV centre-of-mass energy in (a) 2015 and (b) 2016.

## 2.2 ATLAS Detector Description

The ATLAS (A Toroidal Large Hadron Collider ApparatuS) detector design, construction and performance has been described in detail previously [8, 9, 10], so what follows in this chapter is a general description of the detector with a focus on the needs of the analysis that is being presented. The ATLAS detector is effectively a large closed cylindrical detector, made up of four key components which sit in concentric rings around the interaction point, where the proton bunches collide. These components are the inner detector, calorimeters, muon spectrometer and the magnets; each of which are described in further detail below. This design is used as each sub-detector measures different quantities and interacts differently to the various range of particles that ATLAS is required to observe, meaning the ATLAS detector is able to identify and measure the key properties of particles that pass through its volume. Figure 2.2 shows a cut-away schematic of the detector and Figure 2.3 shows a slice of the detector in the plane perpendicular to the beam-pipe, overlaid are simplified illustrations how the detector can respond to a range of particles [11].

### 2.2.1 ATLAS Co-ordinate System

Firstly, to describe the detail of the ATLAS detector there must be a description of the co-ordinate system that is used. ATLAS uses a right-handed coordinate system, in which the origin lies at the interaction point. The  $x$ -axis points to the centre of the LHC ring

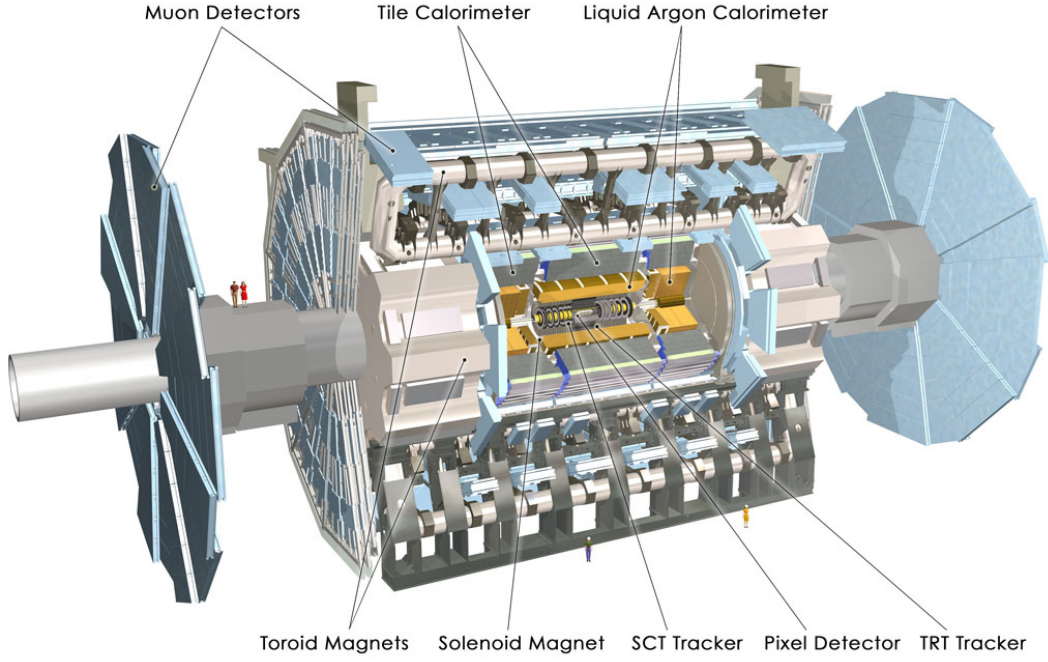


**Figure 2.2:** A cut-away schematic of the ATLAS detector.

parallel to the surface of the earth, the  $y$ -axis points towards the surface of the earth and the  $z$ -axis runs along the beam-pipe, pointing anti-clockwise along the LHC beam-pipe. The azimuthal angle,  $\phi$ , is defined right-handedly around the  $z$ -axis starting at the  $x$ -axis.

The polar angle,  $\theta$ , is defined as the angle measured from the  $z$ -axis, such that along the  $z$ -axis corresponds to  $\theta = 0$  and anti-aligned with the  $z$ -axis corresponds to  $\theta = \pi$ . However, to define the angular direction with respect to the  $z$ -axis the ATLAS co-ordinate system uses pseudo-rapidity,  $\eta$ , instead of using  $\theta$ , for reasons that will be outlined below.  $\eta$  is defined as a function of  $\theta$ :

$$\eta = -\ln \left[ \tan \left( \frac{\theta}{2} \right) \right] \quad (2.1)$$

Thus,  $\eta = 0$  corresponds to a particle travelling perpendicular to the beam-pipe, where a positive value of  $\eta$  corresponds to a particle travelling with a tilt towards the  $z$ -axis. The quantity is called pseudo-rapidity as in the massless limit ( $\lim_{E \rightarrow |\vec{p}|}$ ) it can be shown that  $\eta$  converges to rapidity,  $y$ , where rapidity is defined as,

$$y = \frac{1}{2} \ln \left( \frac{E + p_z}{E - p_z} \right) \quad (2.2)$$

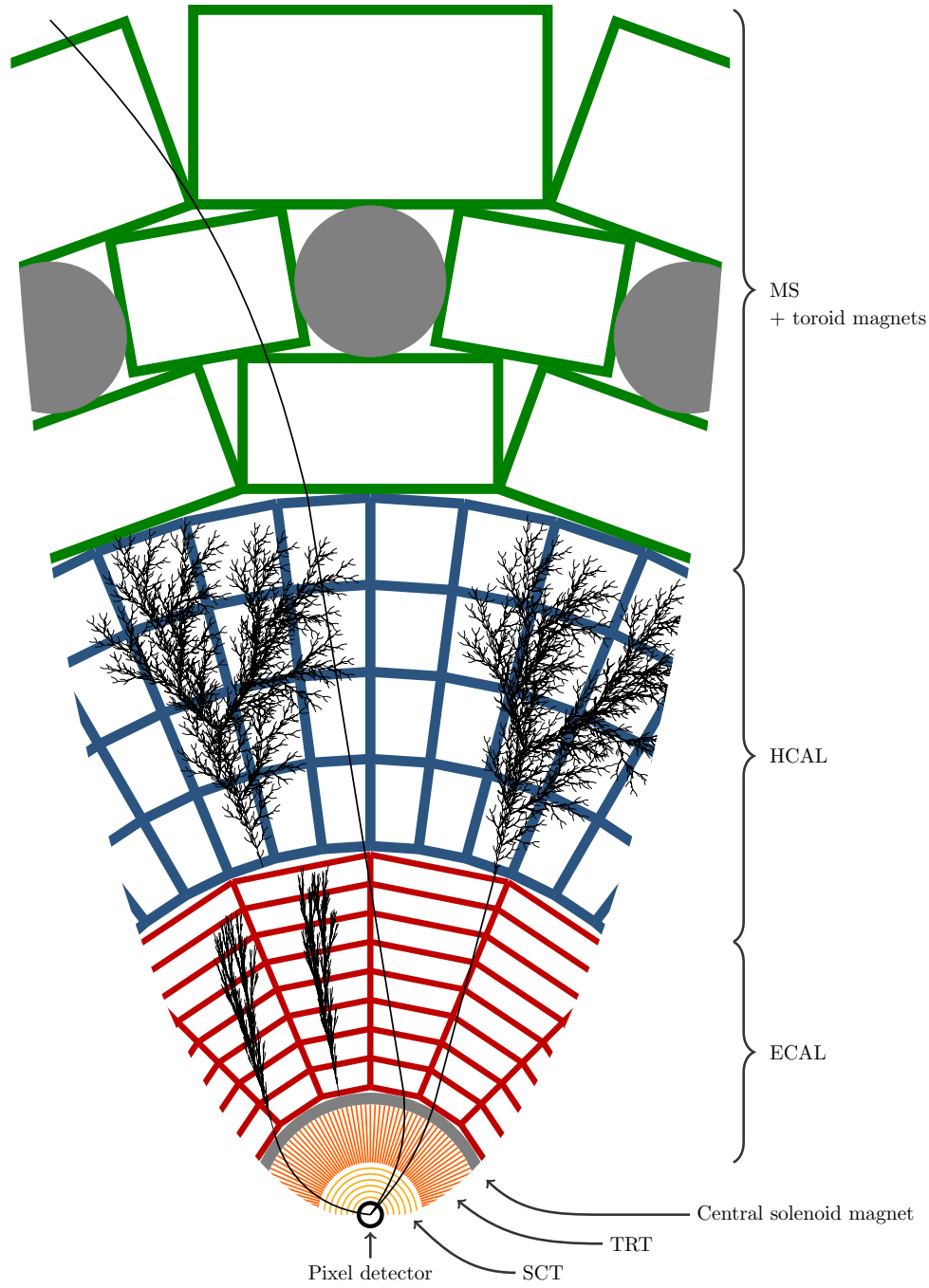


**Figure 2.3:** A visualisation of the ATLAS detector and the various sub-detectors. The view is taken as a slice in a plane perpendicular to the beam-pipe, showing the radial range from the beam-pipe to the edge of the detector. Overlaid are simplified illustrations of how various types of particles interact with the ATLAS detector; specifically from left to right the particles are an electron, a chargeless hadron (e.g. a neutron), a photon, a muon and a charged hadron (e.g. proton). The sub-detector components are not to scale.

A key property of rapidity is that the differences in rapidity,  $\Delta y$ , are invariant against Lorentz boosts along the  $z$ -axis. Thus,  $\eta$  is the final variable chosen in the ATLAS co-ordinate system due to the relation of  $\eta$  with both  $\theta$  and  $y$  and the above mentioned property of  $\Delta y$ . One final quantity commonly used within ATLAS is the variable  $\Delta R$ , which is defined as

$$\Delta R = \sqrt{\Delta\eta^2 + \Delta\phi^2} \quad (2.3)$$

$\Delta R$  represents an angular separation between two vectors within the ATLAS co-ordinate system.

Now that we have discussed the ATLAS co-ordinate system, we can provide a description of the components of the ATLAS detector.

### 2.2.2 Inner Detector

The Inner Detector (ID), the innermost sub-detector on ATLAS, measures the trajectory of charged particles passing through the detector. The ID is constructed from many concentric layers of detector, and as a charged particle passes through the detector each of the layers provides a position measurement, known as a hit. Then using the hits from the many layers the trajectory of the particle can be determined; the measured trajectory is known as a track. The ID is immersed in a 2 T magnetic field which bends the particle's trajectories; from the sign and magnitude of the track's curvature the charge and momentum of the particle can be inferred. The ID is made of three main component parts; the pixel detector, the Semi-Conductor Tracker (SCT) and the Transition Radiation Tracker (TRT), as visualised in Figure 2.4. The ID consists of the barrel, which are made up of cylinders surrounding the beam-pipe to cover low absolute values of  $\eta$ , and the end-caps, which lie perpendicular to beam-pipe on either end of the barrel to cover large values of absolute  $\eta$ : here the description focuses on the barrel as this covers the  $\eta$  range considered by the analysis.

The innermost component of the ID is the silicon pixel detector; in the barrel this detector consists of 4 high-granularity layers of silicon based pixel modules surrounding the beam pipe, covering a range of  $-2.5 < \eta < 2.5$  and a radial distance of 33 mm to 122.5 mm [12, 13]. The high-granularity of the pixel layers, allows for high precision measurements,

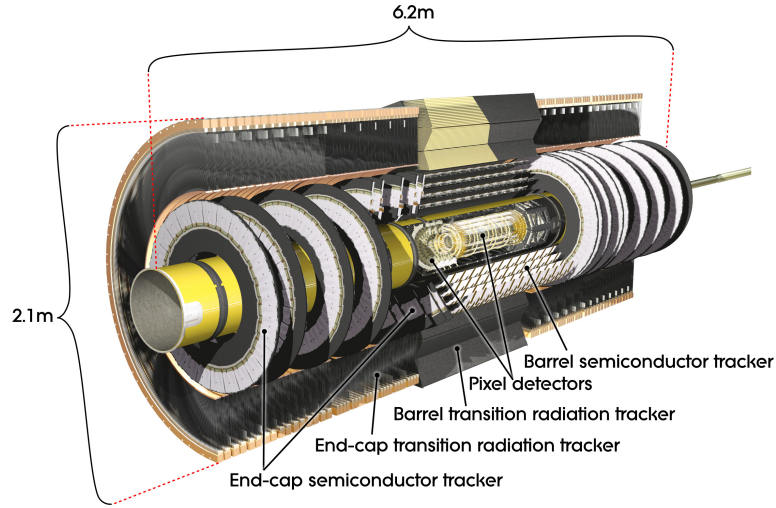


**Figure 2.4:** A cut-away schematic of the ATLAS Inner Detector (ID).

with an intrinsic resolution of approximately resolution of  $\sim 10\mu\text{m}$  in  $R - \phi$  plane and  $\sim 115\mu\text{m}$  in the  $z$ -direction.

Moving radial outwards the next component of the ID is the Semi-Conductor Tracker; which, in the barrel, comprises of 4 cylindrical layers of silicon micro-strips covering a range of  $-2.5 < \eta < 2.5$  and a radial distance of 299 mm to 514 mm. The SCT has an intrinsic resolution of  $\sim 17\mu\text{m}$  in  $R - \phi$  plane and  $\sim 580\mu\text{m}$  in the  $z$ -direction.

The outermost component of the ID is the Transition Radiation Tracker (TRT) constructed of many 4 mm radius tubes filled with xenon. As a charged particle passes through the gas, it will cause ionisation allowing a measurement of its position using drift-time. In the barrel, each tube provides a measurement in the  $R - \phi$  plane with an intrinsic resolution of  $130\mu\text{m}$  and the TRT will typically provide 36 hits per track. In addition to a position measurement, due to the choice of the material between the tubes, a particle passing through the detector will radiate photons at an intensity inversely correlated to the mass of that particle, providing additional information for particle identification.

The trajectory, momentum and charge measurements provided by the Inner Detector are essential for particle identification in ATLAS. In particular, the high precision measurements close to the beam-line allow for vertex reconstruction, which is essential for



identification of tracks coming from B or C hadrons, and hence the identification of  $b$ -jets. This process, known as  $b$ -tagging, is discussed further in Section ??(object definition and selection) and is important within the context of this analysis.

### 2.2.3 Calorimeters

The ATLAS calorimeter, located on the outside of the magnet solenoid surrounding the ID, is designed to provide an energy measurement of the traversing particles. Accurate energy measurements are essential for a good resolution of the mediator mass reconstructed from its decay products, which is important within the context of the analysis being presented in this thesis.

The calorimeter at ATLAS is made up of two different systems that are built in concentric rings; the inner-most is the Electromagnetic Calorimeter system (ECAL), which is used to measure electromagnetic objects such as photons and electrons. Outside of that is the Hadronic Calorimeter system (HCAL), designed to provide an energy measurement of hadronic material. The HCAL is built from the Tile and Hadronic Endcap calorimeters. Both the ECAL and HCAL have barrel and end-cap components to make energy measurements at a large range of  $\eta$  values. Figure 2.5 shows a cut-away of the ATLAS calorimeter.

Below I provide a more detailed description of the calorimeter components; however, the principle behind each detector is common so is described first. The calorimeters at ATLAS are sampling calorimeters, which means they consist of alternating layers of absorber and active material. The role of the absorber layer is to force the particle, whose energy we want to measure, to emit secondary particles. These secondary particles will again emit further particles and so on meaning a “particle cascade” is formed. The role of the active material layer is to measure the energy of the many resulting particles from the cascade, known as the cascade particles. The ATLAS detector is built such that the initial particle will cascade within the volume of the calorimeter system and then, from a measurement of the energy of all the cascade particles, the energy of the initial particle can be inferred.

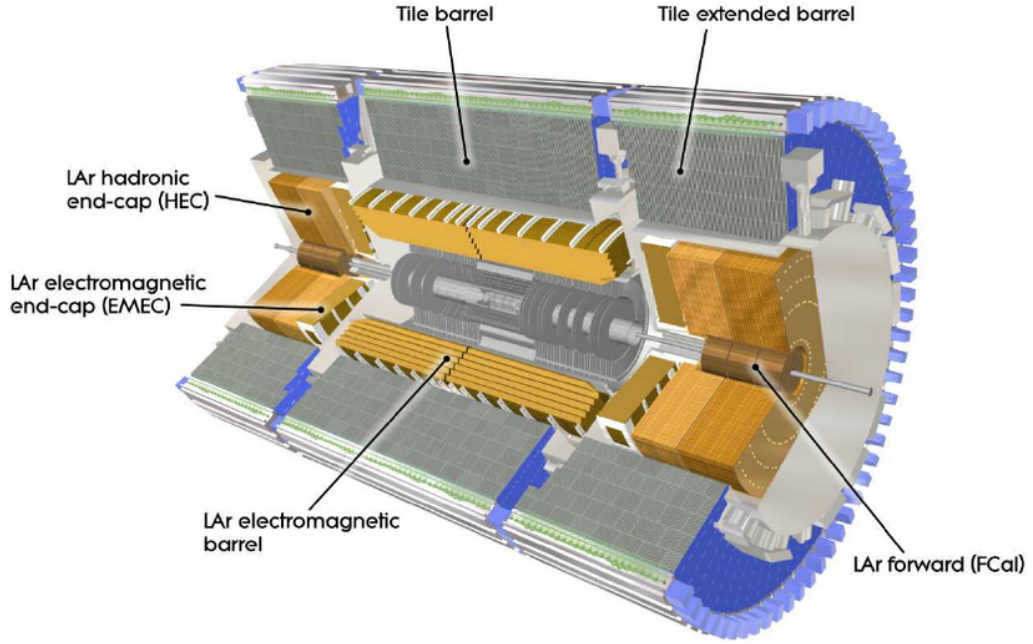


**Figure 2.5:** A cut-away schematic of the ATLAS calorimeter system.

### 2.2.3.1 Electromagnetic Calorimeter (ECAL)

For the electromagnetic interaction, at energies  $\sim \geq 1$  GeV the particle cascade process is mainly caused by two processes; bremsstrahlung, ( $e^{+/-} \rightarrow e^{+/-} + \gamma$ ) and pair production ( $\gamma \rightarrow e^+ + e^-$ ). The electromagnetic calorimeter at ATLAS is known as the Liquid Argon (LAr) calorimeter. The absorber material used in the LAr calorimeter is lead, due to its large density of charged particles (high Z) which increases the rate of the cascade processes. The active material is liquid argon; when a cascade particle passes through the liquid argon it causes ionisation, and the released electrons are captured using an electric field. The number of released electrons is proportional to the energy of the cascade particle, meaning that the energy of the cascade particle can be measured.

As discussed above the LAr is split up into two sections; the barrel section covers a region of  $|\eta| < 1.475$  and two end-cap components cover  $1.375 < |\eta| < 3.2$ . The depth of an electromagnetic calorimeter is often expressed in terms of the radiation length,  $X_0$ , which is the distance that an electron's energy reduces by a factor of  $e^{-1}$  through bremsstrahlung, or  $7/9$  of the mean free path for a photon to pair produce electrons. It is worth noting that this quantity is strongly material dependant; a high-Z material, such as lead, has a shorter

$X_0$ . The LAr calorimeter has a depth of  $> 22 X_0$  in the barrel and  $> 24 X_0$  in the end-caps, meaning that almost all of the particle shower from a high-energy photon or electron can be contained within electromagnetic calorimeter.

### 2.2.3.2 Hadronic Calorimeter (HCAL)

If a particle can also interact through strong interactions, such as the components of a hadronic jet, then the particle cascade is a more complicated process. A hadronic cascade processes is dominated by processes such as ionisation, nuclear spallation and neutron generation [14, 15]. For a chargeless hadron, for example a neutron, strong processes, such as spallation, are the only processes that contribute to its cascade. During these hadronic cascade processes many  $\pi_0$  mesons are made, which can decay to a pair of photons and thus form electromagnetic cascade as described above.

For hadronic interactions, the size of detector is measured by the interaction length,  $\lambda$ , defined as the distance required to reduce the number of relativistic hadrons by  $e^{-1}$ . This means that by the end of the LAr calorimeter there is  $2.3 \lambda$  of active material in the barrel, so the full hadronic shower cannot be captured by the LAr calorimeter alone. For a full measurement of the hadronic energy, the Hadronic Calorimeter system (HCAL) is required.

The Tile Calorimeter is constructed from absorber layers of steel and active material layers of scintillating tiles, and has a depth of  $7.4 \lambda$ , meaning the majority of the hadronic shower can be captured by either the LAr calorimeter or the Tile calorimeter. The Tile Calorimeter is split up into the barrel and the extended barrel components; the barrel covers the region  $|\eta| < 1.0$  and the extended barrel covers the region  $0.8 < |\eta| < 1.7$ .

To cover the more forward regions there are two more calorimeter detectors. The Hadronic Endcap Calorimeter (HEC) is housed in two large wheels at either end of the ATLAS detector and covers a region of  $1.5 < \eta < 3.2$ . The HEC is a sampling calorimeter built using copper as the absorber layers and liquid argon as the active material and has a depth of  $\sim 12 \lambda$ . In addition the Forward Calorimeter (FCAL) covers the very forward region of  $3.1 < \eta < 4.9$ , which is outside the range considered within this analysis. It is constructed from absorber layers of copper (for EM interactions) and tungsten (for hadronic

interactions) with liquid argon for the active material layers.

Another important point about the ATLAS calorimeter is that it is non-compensating calorimeter; that is to say that the response of the detector to an electromagnetic particle (such as an electron) is larger than the response of a hadronic particle (for example a pion). The reason for this is some energy is lost in hadronic cascade process; mainly due to the energy required to release nucleons from calorimeter nuclei during spallation, but also from the recoil energy given to the calorimeter nuclei and neutrinos created during strong processes that can escape the calorimeter [16, 17]. To account for the fact that the ATLAS calorimeter is non-compensation, calorimeters are calibrated to the EM-scale and then a jet energy scale correction is applied, this process is described further in Section ??(object definition and selection).

#### 2.2.4 Muon Spectrometer

The only standard model particle visible to ATLAS which can pass through the calorimeter is the muon; hence to identify and obtain the momentum of muons an additional detector, the Muon Spectrometer (MS), is used. The MS is a detector which surrounds the hadronic calorimeter, measuring the momentum of muons by observing the curvature of their trajectories in magnetic fields. Trajectories are determined using muon position measurements from multiple layers of detectors, analogous to what has been described for the inner detector.

In the barrel region ( $|\eta| < 1.4$ ) the large barrel toroid provides the magnetic field, in the end-cap region ( $1.6 < |\eta| < 2.7$ ) the two smaller end-cap magnets provide the magnetic field and finally in the transition region ( $1.4 < |\eta| < 1.6$ ) both sets of magnets contribute to the magnetic field. A further description of the magnets used in ATLAS is found in the next section.

Muon chambers are the detectors tasked with providing the muon position measurements required to reconstruct muon tracks. The muon chambers come in two types; trigger and precision. The trigger muon chambers provide a quick position measurement in 3-dimensions which can be used to identify muons tracks in the trigger. The trigger muon

chambers cover a range  $|\eta| < 2.0$ ; consisting of Resistive Plate Chambers (RPCs) in the barrel and Thin Gap Chambers (TGCs) in the end-cap regions. The precision muon chambers provide a precise measurement of the muon position co-ordinates in the  $R - z$  plane, the plane in which track curvature occurs in the muon spectrometer, allowing for precise measurements of the muon track- $p_T$ . In the barrel region, precision muon chambers are arranged in three concentric cylindrical layers of chambers formed around the beam-pipe, whilst in the transition and end-cap regions there are three layers of chambers either side of the barrel lying in disks perpendicular to the beam-pipe. In the region  $|\eta| < 2.0$ , the precision muon chambers are made from Monitored Drift Tubes (MDTs), whilst at large pseudo-rapidities ( $2.0 < |\eta| < 2.7$ ), Cathode Strip Chambers (CSCs) are used.

There is an additional use of the muon spectrometer that relates to high-energy jets. Whilst for most jets their shower is fully contained within the calorimeter there are some jets, particularly at high- $p_T$ , where a non-negligible fraction of energy from the shower goes beyond the calorimeter. This effect, known as ‘punch-through’, is accounted for using energy deposits in the muon spectrometer.

### 2.2.5 Magnets

In ATLAS magnetic fields are important for obtaining the momentum and charge of particles from their observed trajectories in the ID and Muon Spectrometer. ATLAS is made up of four large superconducting magnets; the inner solenoid which surrounds the inner detector and provides a 2 T magnetic field within the ID. The barrel toroid magnet provides a magnetic field of up to 2.5 T in the central regions of the muon spectrometer and the two end-cap toroid magnets which produce a magnetic field of up to 3.5 T in the forward regions of the MS. Figure 2.6 shows the layout of the magnets in ATLAS [18].

## 2.3 Trigger

In 2015 and 2016, the LHC has been colliding proton beams with a spacing of 25 ns, meaning that the ATLAS experiment has been taking data at a rate of 40 MHz. However, due to the large computing resources required to process and store each event, it is not possible to record all this data for use in an analysis. To resolve this problem, the ATLAS experiment

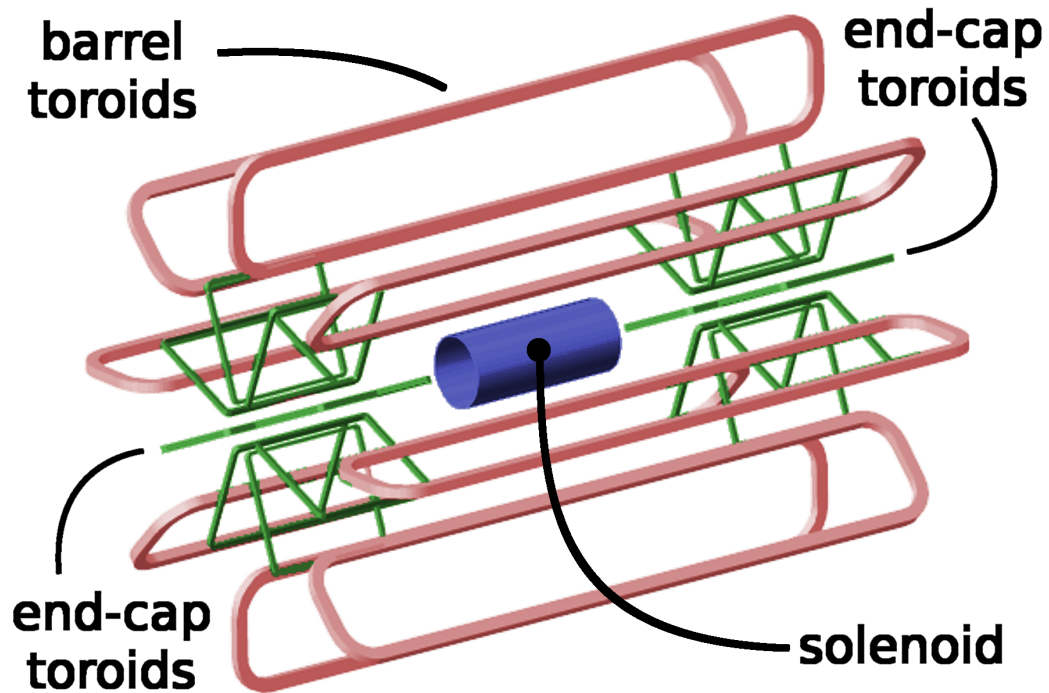


**Figure 2.6:** The layout of the ATLAS magnets.

uses a trigger system to reduce the event rate by selecting the events of interest that contain high- $p_T$  physics objects, which indicate that a hard scatter has occurred in that event.

The ATLAS trigger-system has two levels; the first level trigger (L1) and the higher level trigger (HLT) [19]. Figure 2.7 shows a schematic outlining the trigger used in Run-2 [20].

The first level trigger (L1) is hardware based which reduces the rate from 40 MHz to 100 kHz within a time window of  $2.2\ \mu\text{s}$ . The L1 trigger uses custom electronics to rapidly process information directly from the calorimeter and the muon spectrometer, searching for high- $p_T$  muon tracks and large calorimeter deposits. The information is then passed to the central trigger which uses a set of pre-defined conditions to decide if a L1 trigger accept is given and thus events are passed on to the next step of triggering. At the same time Regions of Interests (ROIs) are constructed around the objects that have fired the L1 trigger, which are passed on to the HLT.

The next step is the HLT, a software based trigger, which further reduces the event

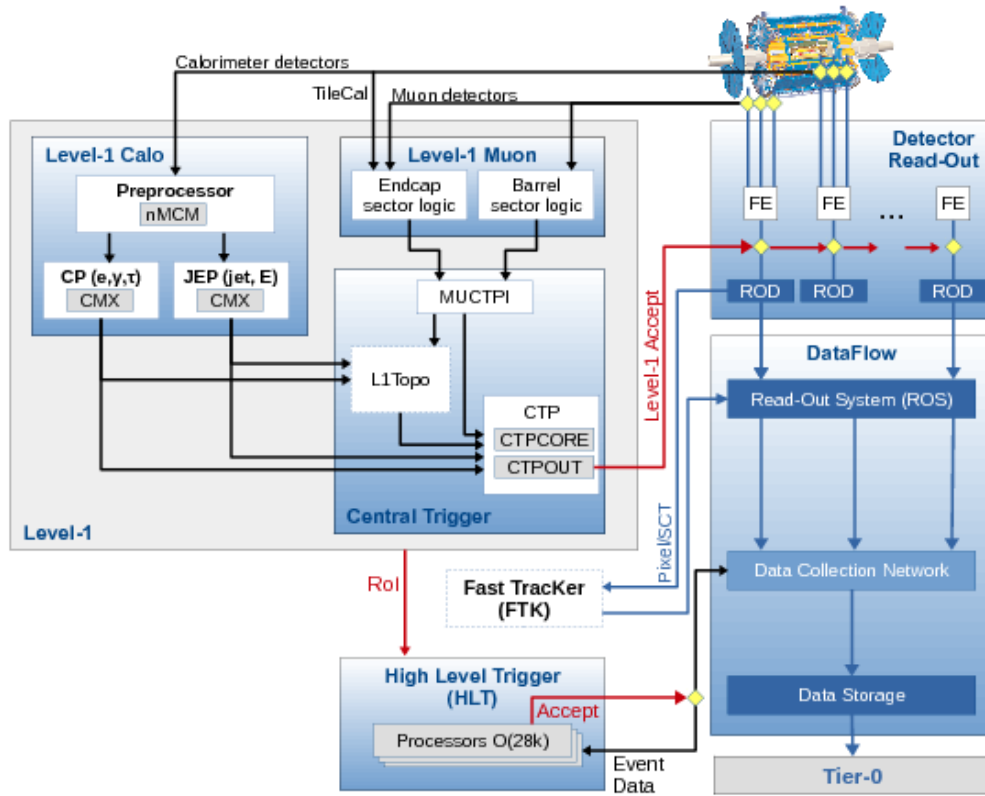


**Figure 2.7:** A schematic of the ATLAS trigger and data-acquisition system in Run-2, with a focus on the components required for triggering.

rate to 1 kHz within a time window of 0.2 s. The HLT uses the information from the full detector to perform a more complete reconstruction of the physics objects within the event, the most time consuming reconstruction algorithms only being run only within the ROIs taken from L1. The more complex event analysis allowed within the software-based trigger includes track reconstruction and therefore allows for  $b$ -jet identification. If the content of the event reconstruction passes a pre-set criteria, a HLT accept is issued meaning that the events are passed on for processing and storage.

A further description of triggers used in the analysis, with a particular focus on the  $b$ -jet trigger performance can be found in ??( $b$ -jet trigger chapter).

## Chapter 3

# Triggering in the di- $b$ -jet analysis

As described in Section 2.3, ATLAS does not have the resources to process or store all the data from the 40 MHz of collisions delivered by the LHC. To solve this problem the ATLAS trigger system performs the vital role of reducing the rate of data-taking to 1 kHz by selecting events containing a high- $p_T$  object.

As a result all analyses must choose a trigger strategy and understand the impact of this trigger on their analysis. In the di- $b$ -jet analysis we use a single jet trigger for the high-mass channel and a double  $b$ -jet trigger for the low-mass channel. This chapter aims to provide a detailed description of the triggers used in this analysis, and as such is organised in the following manner; Section 3.1 provides a brief description of jet triggers as used in the high-mass channel and the limitations of this approach, Section 3.2 contains a description of  $b$ -jet triggers that are used in the low-mass channel and finally Section 3.3 presents the measurement of the  $b$ -jet trigger efficiency, an essential input of the low-mass channel.

## 3.1 Jet-Triggers

Jet-triggers are tasked with selecting events with one or more jets from the deposits in the ATLAS calorimeter system, this is one of most challenging triggers in any hadron-hadron collider due to extremely high cross-sections of hadronic jet production [21]. In Run-2 the jet-triggers are used at both L1 and HLT level; each using different levels of information and different algorithms, so are described separately within this section.

### 3.1.1 Level 1

The L1 trigger is a hardware based trigger which accepts or rejects an event within  $2.2\,\mu\text{s}$ . The L1 jet-trigger receives trigger towers from the calorimeter; where a trigger tower is the



measured energy deposit in a cell of the ECAL or HCAL of granularity  $0.1 \times 0.1$  in the  $\eta - \phi$  plane. In the L1 trigger hadronic jet algorithms search for a neighbouring group of  $4 \times 4$  trigger towers containing energy deposits above some pre-set threshold. Our analysis uses the L1 trigger known as `L1_J100`, which requires that at least one trigger tower group with an energy deposit of 100 GeV has been found. Other L1 triggers that search for multiple clusters are also possible to reduce the energy thresholds required. The L1 trigger can then seed the HLT trigger. It is also worth noting that at L1 there is no tracking information, meaning that electron and taus are also triggered on using similar techniques as hadronic jet algorithms, except using narrower groups of trigger towers.

### 3.1.2 HLT

The HLT trigger is a software based trigger which, due to the lower input rate and larger time window, is able to use more complex algorithms to reconstruct jets. At the HLT level jets are reconstructed using topoclusters (TCs) constructed from neighbouring cells selected using the cell's energy significance ( $E/\sigma$ ); TCs are seeded from cells with  $E/\sigma > 4$ , then neighbouring cells with  $E/\sigma > 2$  are added and finally all neighbouring cells around are also added. Jets are then reconstructed from the topoclusters; in this analysis we use jets that have been reconstructed using the anti- $k_T$  algorithm with an  $R = 0.4$ <sup>1</sup>.

### 3.1.3 High-mass trigger selection

For the high-mass analysis we use the trigger `HLT_j380`, that is fired when a jet is found with a  $p_T > 380$  GeV. This is chosen as it is the lowest un-prescaled single jet-trigger; meaning that of triggers that accept every event passing a single jet criteria, this trigger has the lowest jet- $p_T$  threshold. Due to the exponential increase in jet production cross-section at low jet- $p_T$ , the  $p_T$  threshold is set to keep the acceptance rates low enough such that the HLT trigger is within its output rate budget of 1 kHz.

However, as will be discussed further in Section ??(sec:evtSel), this  $p_T$  threshold limits the high-mass di- $b$ -jet analysis to only select events with  $m_{jj} > 1.2$  TeV, otherwise the  $m_{jj}$  range will enter a kinematic region where trigger acceptance is less than 1 in such a way that the QCD background is sculpted in a manner that the background modelling can not adapt to. To reach to lower masses a different trigger strategy is required.

---

<sup>1</sup>Section ?? (sec:obj-jets) defines these terms

## 3.2 *b*-Jet Triggers

In this analysis we search for pairs of *b*-jets, which, as described in Section ??(sec:obj-bjets), can be identified from the topology of tracks in the inner detector indicating that a *B*-hadron was within the jet. This additional selection at the trigger level reduces rates significantly<sup>2</sup> allowing a lower jet- $p_T$  threshold than was used by the single jet- $p_T$  trigger, and hence lower  $m_{jj}$  values to be accessed. *b*-jet triggers have been used in a range of previous ATLAS analyses, including for HH to 4 *b*-jets [22].

### 3.2.1 General description

In 2016 data, the *b*-jet trigger configuration contains three steps [23], making use of the regions of interest (RoI) described by the jets found by the jet-trigger. Firstly, a ‘fast’-tracking algorithm is run in a super-RoI which is formed around all jets in the event which have  $E_T > 30$  GeV; these tracks are then used to identify the primary vertex in the event. Secondly, within each jet RoI precision tracking is run, with a constraint on the PV position from the first step. Finally, these tracks are the input to the multi-variate *b*-tagging algorithm described in Section ??(sec:obj-bjets\_MV2) to identify *b*-jets. There are several *b*-jet triggers available in the ATLAS trigger menu; with a variety of requirements on the jet multiplicity, number of tagged jets and *b*-tag operating point used. Figure 3.1 shows ROC curves representing the expected performance of Run-2 *b*-trigger.

There are few subtleties worth commenting on the *b*-jet trigger configuration, which affect decisions taken in this analysis. One is that on this figure we see two lines corresponding to different *b*-tagging algorithms used in *b*-jet trigger; IP3D+SV1 was used in 2015 data-taking, whilst the MV2c20 was used in 2016 data-taking. Another difference between 2015 and 2016 is the primary vertex finding algorithm used; 2016 data-taking employed a more complicated algorithm based on what is used offline, known as *xPrmVtx*, whilst in 2015 an algorithm using a simple histogram based approach was employed, known as *EFHist*.

---

<sup>2</sup>It is known that the QCD background is dominated by light-jets, see Figure ??Plot of background flav comp

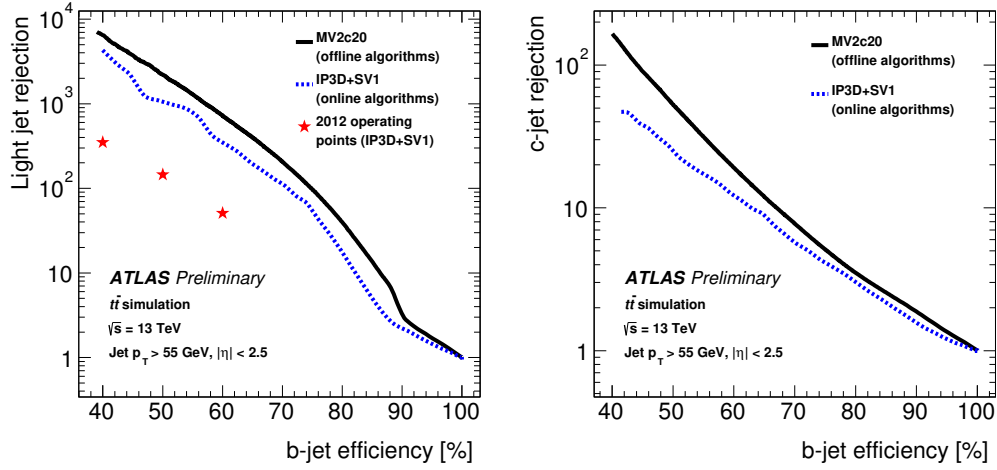


**Figure 3.1:** The expected  $b$ -jet efficiency of  $b$ -jet triggers with respect to (a) light-jet and (b)  $c$ -jet rejection in the case where the  $b$ -tagging algorithm used is MV2c20 (Black), IP3D+SV1 (Blue) and for the set-up used in Run-1 (red stars).

Finally it is worth noting that there are differences between online and offline  $b$ -tagging that will have an impact on what is to follow. Firstly, coarser tracking information is available online, notably online tracks are not reconstructed from the whole range of the detector. Secondly, a slightly different training setup is used for the multi-variate algorithm, mainly that a different fraction of  $c$ -jets were present in the training sample (10% offline vs. 20% online).

In this analysis we use the double  $b$ -jet trigger,

$$\text{HLT\_j150\_bmc2c2060\_split\_j50\_bmvc2c2060\_split}$$

which triggers on two jets with  $p_T > 150$  and 50 GeV respectively, which have been  $b$ -tagged at the 60% efficiency working point.

### 3.3 Efficiency Measurement of the $b$ -Jet Trigger

Any part of the ATLAS detector framework needs to be understood and calibrated with data for use in an analysis; and this includes the trigger which can have a large impact on the analysis. In this section I discuss the strategy and results of the  $b$ -jet trigger measurement in 2016, which is an important input to the low-mass channel of the di- $b$ -jet analysis.

### 3.3.1 Strategy

The  $b$ -jet trigger is always used in tandem with offline  $b$ -tagging which is calibrated independently of the  $b$ -trigger. Hence, to do this measurement whilst making use of the offline  $b$ -tagging calibrations already available, we measure the  $b$ -jet trigger efficiency with respect to offline  $b$ -tagging,  $\epsilon_{bTrig}$ , which is defined as the number of offline-tagged true  $b$ -jets that match an online-tagged trigger-jet by the number of offline tagged  $b$ -jets that match a trigger jet. Or to put this in an equation;

$$\epsilon_{bTrig} = \frac{N(\text{Offline-tagged, online-tagged, true } b\text{-jets})}{N(\text{Offline-tagged, trigger-matched, true } b\text{-jets})} \quad (3.1)$$

This quantity can be interpreted as the probability that a true  $b$ -jet is tagged at the trigger-level, given that there is a jet at the trigger level and that it would be  $b$ -tagged at the offline stage.

To measure  $\epsilon_{bTrig}$  we require a sample that has high  $b$ -jet purity, such that we have confidence that the jets we use to calculate this ratio are true  $b$ -jets. We also need to be able to trigger on this sample in such a way that we are not biasing ourselves from using  $b$ -tagging online; or simply put we cannot use the  $b$ -jet trigger to select events. The sample we use to fill these criteria is a di-lepton  $t\bar{t}$  sample containing a muon and an electron. Top-quarks decay to a  $W$ -boson and a  $b$ -quark with almost 100% branching ratio meaning that this sample provides a good source of  $b$ -quarks, but also the electron and muon give a distinct signature which allows us to select this process with good purity and gives a non- $b$ -jet object to trigger on. The exact event selection is described below.

The  $b$ -jet trigger efficiency is determined in data and is compared to the efficiency found in a simulated  $t\bar{t}$  sample which is used to extrapolate the efficiency to higher jet- $p_T$  where the data-derived efficiency loses statistical precision. The efficiency in data, including the simulation based extrapolation, can then be compared to simulation to derive a Data/Monte-Carlo scale factor, which is used as the input to the analysis.

$\epsilon_{bTrig}$  and Data/Monte-Carlo scale factors are derived for all combinations of offline and online  $b$ -tagging working points. However, we will show the process for the 70% offline and 60% online working point as this is set of working points used in this analysis.

### 3.3.2 Datasets

The data used for this analysis is the full 2016 ATLAS data-set. In addition to the usual data-quality requirements applied, as discussed in Section ??(sec:evtSel\_GRL), a  $b$ -jet trigger aware Good Run List (GRL) <sup>3</sup> applies the requirement that the online beamspot is within 2mm of the origin in Periods A-I of the data. This means that the data-set contains  $24.5 \text{ fb}^{-1}$  of data. A discussion of the requirement for this GRL is in Section 3.3.5.

For the simulated  $t\bar{t}$  sample, the generation is performed with a Powheg-Box v2 [24] generator with the CT10 PDF sets in the matrix element calculations is used. We will also consider a simulated single-top sample; electroweak t-channel, s-channel and  $Wt$ -channel single top-quark events are generated using the Powheg-Box v1 generator. This generator uses the 4-flavour scheme for the NLO matrix elements calculations together with the fixed four-flavour PDF set CT10f4. The parton shower, fragmentation, and the underlying event are simulated using Pythia6.428 [25] with the CTEQ6L1 [26] PDF sets and the corresponding Perugia 2012 tune (P2012) [27]. The top mass is set to 172.5 GeV. The EvtGen v1.2.0 program [28] is used for properties of the bottom and charm hadron decays.

### 3.3.3 Event Selection

A high-purity sample of  $b$ -jets is selected using a di-lepton  $t\bar{t}$  selection.

The event selection is summarised as follows:

- The event fired a single lepton bperf trigger which are:
  - HLT\_mu26\_imedium\_2j35\_bperf
  - HLT\_e26\_tight\_iloose\_2j35\_bperf
  - HLT\_e26\_lhtight\_iloose\_2j35\_bperf
- At least 1 medium muon:  $p_T > 25 \text{ GeV}$ , which has no jet within a  $\Delta R$  of 0.4.
- At least 1 medium electron:  $p_T > 25 \text{ GeV}$ .
- 2 offline  $b$ -tagged jets:
  - Offline  $R=0.4$  anti- $k_T$  jets.
  - $p_T > 35 \text{ GeV}$  and  $|\eta| < 2.5$ .
  - Offline  $b$ -tagged at the 85% operating point.

---

<sup>3</sup>A GRL is effectively a list of lumi-blocks that pass certain data-quality requirements. As mentioned in the text a further discussion is held here in Section ??(sec:evtSel\_GRL)

- Jet must be matched to a trigger-jet.

Descriptions of the object-definitions of muons, electrons, jets and  $b$ -tagged can be found in Sections ??(sec:object\_muon), ??(sec:object\_elec), ??(sec:object\_jet) and ??(sec:object\_bjet) respectively. Online trigger jets are matched to offline jets using  $\Delta R$  matching, requiring for a match the jets must have  $\Delta R < 0.6$ .

The triggers used are bperf trigger, which are special triggers used in data-taking specifically for monitoring the  $b$ -jet trigger performance. They fire if a muon or an electron with  $p_T > 26 \text{ GeV}$  is reconstructed at the trigger level. The bperf triggers then run the online  $b$ -tagging algorithm on all trigger jets with  $|\eta| < 2.5$  and  $p_T > 35 \text{ GeV}$  without performing any cuts on the output of the multi-variate algorithm; ensuring there is no bias in the efficiency measurement.

### 3.3.4 The Initial Problem

To give context to the following section; the first discussion will be what was first observed when measuring the  $b$ -jet efficiency. Figure 3.2 shows  $\epsilon_{b\text{-}Trig}$ , when no  $b$ -jet trigger aware GRL is not applied and no requirement on offline jets matching a trigger jet is required in the denominator. In addition we can see that there is a clear shape in the jet- $\eta$  distributions that needs to be understood. This shows the efficiency in data is substantially below the efficiency expected from simulation, an effect that needs to be investigated and understood properly.

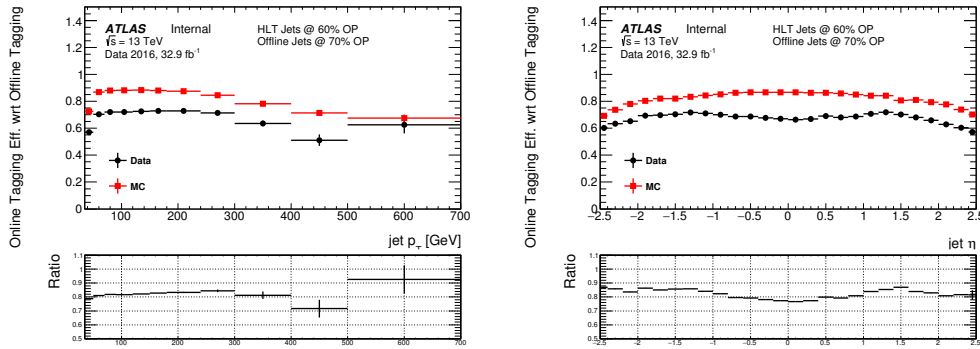


**Figure 3.2:** The 60%  $b$ -jet trigger efficiency with respect to an offline 70% operating point tag for data from Data (black) and simulation (red) against jet- $p_T$  (left), jet- $\eta$  (right). The  $b$ -trigger aware GRL is not applied and trigger matching is not required.

### 3.3.5 Investigation and Solution

Given the disagreements between data and simulation we performed a number of cross-checks to understand this discrepancy, including period dependance, detector performance, pile-up conditions and online beamspot position performance. In this section, I summarise the results of the investigation and demonstrate the  $b$ -trigger performance in 2016 data.

As described above, in 2016 data an algorithm known as  $xPrmVtx$  was used. It has since been uncovered that there was a bug in the code used to implement this algorithm; effectively different co-ordinates were used by components of the code. Online tracks passed to  $xPrmVtx$  use position with respect to online beam-spot position, where the  $xPrmVtx$  algorithm assumed track position with respect to the origin. This means that when the online beam-spot  $z$ -position is far from the origin, a vertex with position at the origin is passed to the  $b$ -tagging algorithms, which leads to sub-optimal performance. This will be shown below.

The exact setup for the  $b$ -jet trigger has changed as data has taken, to respond to performance issues as they are noticed and patches are applied. As such the relevant conditions of the  $b$ -jet trigger can be split into three regions of data-taking, which I will refer to as epochs, and the effect of  $xPrmVtx$  returning a dummy vertex on  $b$ -jet trigger performance is different in each of these epochs. Table ?? summaries the effect on the  $b$ -jet trigger of not finding a valid  $xPrmVtx$  vertex on the  $b$ -jet trigger in each epoch. As a result of these differences in trigger performance, each epoch is now considered studied independantly.

Epoch	Runs	Periods	Effect if no $xPrmVtx$ PV is found
1	296939-300571, 300655	A,B(part)	An invalid vertex is used by the online $b$ -tagging resulting in very low $\epsilon_{bTrig}$
2	300600, 300784-308084	B(part),C,D,E,F,G,I,J	The $b$ -jet trigger is not fired
3	309331-311481	K,L	A back-up primary vertex finding algorithm is used.

**Table 3.1:** A table describing the effect of not finding a valid  $xPrmVtx$  primary vertex on different epochs of data.

In Epoch 1, due to the use of an invalid vertex, as described in Table ??, there is a

lower  $\epsilon_{bTrig}$  compared to that measured in simulation, as shown in Figure 3.3 for Epoch 1. The variable vertex class, shown in Figure 3.3, is defined as 0 when a valid xPrmVtx vertex is found and 1 if not.

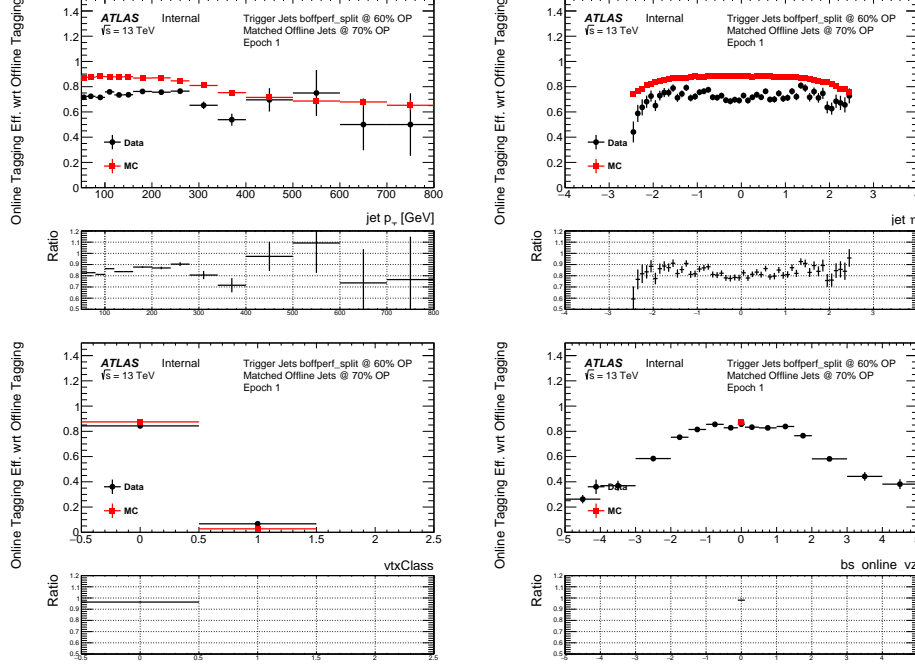


**Figure 3.3:** The 60%  $b$ -jet trigger efficiency with respect to an offline 70% operating point tag for data from Epoch 1 (black) and simulation (red) against jet- $p_T$  (upper left), jet- $\eta$  (upper right), vertex class (lower left) and online beamspot  $z$ -position (lower right).

For Epoch 2, due to the  $b$ -jet trigger not firing when an xPrmVtx PV is not found, as described in Table ??, we find that there are no online  $b$ -tagged jets for some events. To account for this, in addition to  $\epsilon_{bTrig}$ , we must measure the  $b$ -perf efficiency,  $\epsilon_{bPerf}$ , the efficiency that there are online jets in an event to match the offline jets.  $\epsilon_{bPerf}$  is calculated by dividing the number of events that pass the trigger HLT\_mu26\_imedium\_2j35\_bperf by the number that pass the trigger HLT\_mu26\_imedium. A lower  $\epsilon_{bPerf}$  efficiency is observed in Epoch 2 than in simulation, as shown in Figure 3.5. However in Epoch 2,  $\epsilon_{bTrig}$  is measured to be in agreement with simulation within 5%.

For Epoch 3, when no xPrmVtx PV is found then a backup PV finding algorithm is used, known as EFHist. EFHist is an algorithm which finds the PV through a basic histogramming of the tracks. Figure 3.6 shows  $\epsilon_{bTrig}$  for Epoch 3 for jet- $p_T$ , jet- $\eta$  and vertex class (as defined above). When a valid xPrmVtx vertex is found (vertex class = 1) then the efficiency in data is comparable to that when an xPrmVtx vertex is found, showing



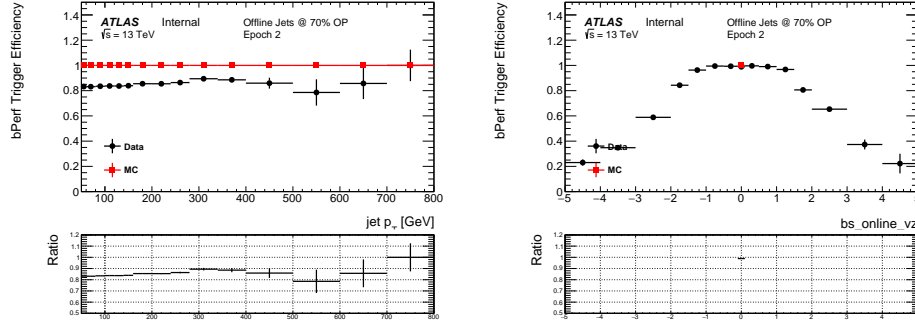


**Figure 3.4:**  $b$ -perf efficiency,  $\epsilon_{bPerf}$ , for data from Epoch 2 (black) and simulation (red) against leading-jet  $p_T$  (left) and online beamspot  $z$ -position (right).

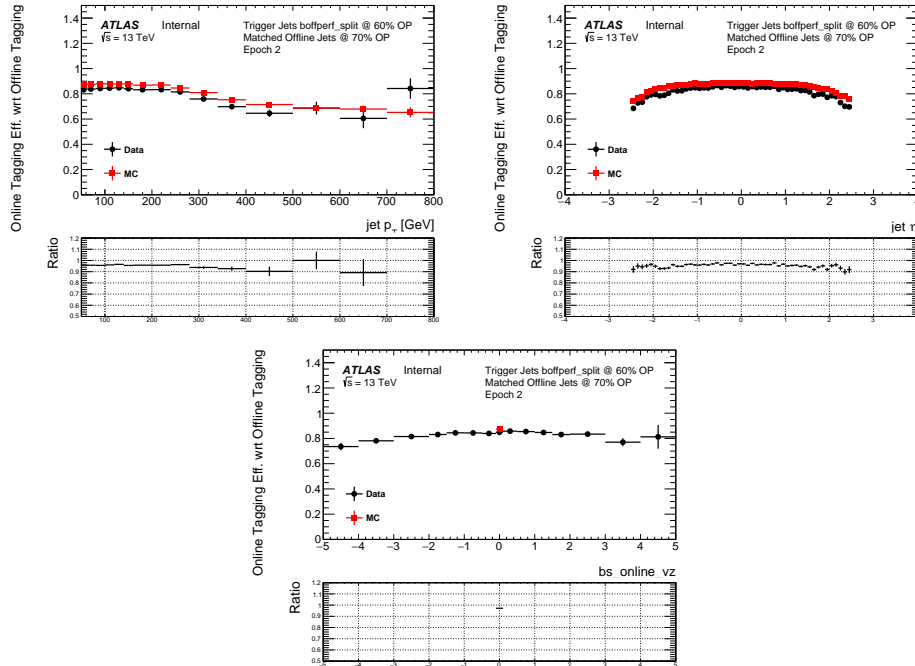


**Figure 3.5:** The 60%  $b$ -jet trigger efficiency with respect to an offline 70% operating point tag for data from epoch 2 (black) and simulation (red) against jet- $p_T$  (left), jet- $\eta$  (right) and online beamspot  $z$ -position (lower).

the success of the backup vertex approach.

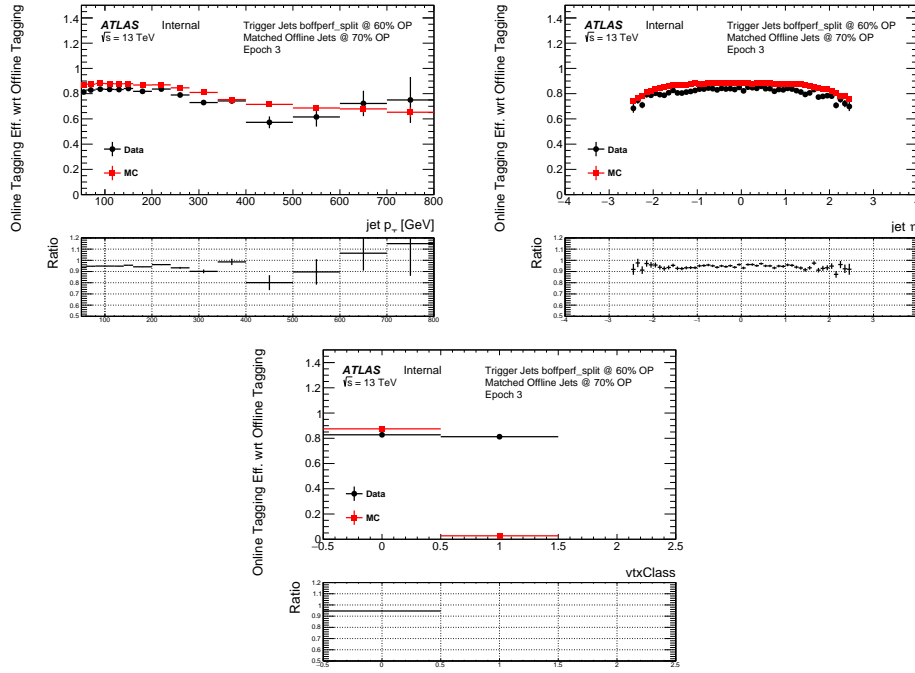


**Figure 3.6:** The 60%  $b$ -jet trigger efficiency with respect to an offline 70% operating point tag for data from Epoch 3 (black) and simulation (red) against  $\text{jet-}p_T$  (upper left),  $\text{jet-}\eta$  (upper right) and vertex class (lower).

### 3.3.6 Measurement and Systematic Assignment

### 3.3.7 Cross-checks

Electron/Muon overlap checks, re-weighting of subleading

## Chapter 4

# General Conclusions

Lorem ipsum dolor sit amet, consectetur adipiscing elit. Etiam lobortis facilisis sem. Nullam nec mi et neque pharetra sollicitudin. Praesent imperdiet mi nec ante. Donec ullamcorper, felis non sodales commodo, lectus velit ultrices augue, a dignissim nibh lectus placerat pede. Vivamus nunc nunc, molestie ut, ultricies vel, semper in, velit. Ut porttitor. Praesent in sapien. Lorem ipsum dolor sit amet, consectetur adipiscing elit. Duis fringilla tristique neque. Sed interdum libero ut metus. Pellentesque placerat. Nam rutrum augue a leo. Morbi sed elit sit amet ante lobortis sollicitudin. Praesent blandit blandit mauris. Praesent lectus tellus, aliquet aliquam, luctus a, egestas a, turpis. Mauris lacinia lorem sit amet ipsum. Nunc quis urna dictum turpis accumsan semper.

## **Appendix A**

# **An Appendix About Stuff**

(stuff)

## **Appendix B**

# **Another Appendix About Things**

(things)

## Appendix C

# Colophon

*This is a description of the tools you used to make your thesis. It helps people make future documents, reminds you, and looks good.*

(example) This document was set in the Times Roman typeface using L<sup>A</sup>T<sub>E</sub>X and BibT<sub>E</sub>X, composed with a text editor.

# Bibliography

- [1] G. Arnison et al. Experimental Observation of Isolated Large Transverse Energy Electrons with Associated Missing Energy at  $s^{1/2} = 540$  GeV. *Phys. Lett.*, 122B:103–116, 1983. [,611(1983)].
- [2] G. Arnison et al. Experimental Observation of Lepton Pairs of Invariant Mass Around 95-GeV/ $c^2$  at the CERN SPS Collider. *Phys. Lett.*, 126B:398–410, 1983.
- [3] M. Banner et al. Observation of Single Isolated Electrons of High Transverse Momentum in Events with Missing Transverse Energy at the CERN anti-p p Collider. *Phys. Lett.*, 122B:476–485, 1983.
- [4] P. Bagnaia et al. Evidence for  $Z_0 \rightarrow e^+e^-$  at the CERN anti-p p Collider. *Phys. Lett.*, 129B:130–140, 1983.
- [5] F. Abe et al. Observation of top quark production in  $\bar{p}p$  collisions with the collider detector at fermilab. *Phys. Rev. Lett.*, 74:2626–2631, Apr 1995.
- [6] S. Abachi et al. Observation of the top quark. *Phys. Rev. Lett.*, 74:2632–2637, Apr 1995.
- [7] Atlas public lumi results run-2. <https://twiki.cern.ch/twiki/bin/view/AtlasPublic/LuminosityPublicResultsRun2>.
- [8] G. Aad et al. The ATLAS Experiment at the CERN Large Hadron Collider. *JINST*, 3:S08003, 2008.
- [9] A. Airapetian et al. *ATLAS detector and physics performance: Technical Design Report, 1*. Technical Design Report ATLAS. CERN, Geneva, 1999.
- [10] G. Aad et al. Performance of the atlas detector using first collision data. *Journal of High Energy Physics*, 2010(9):56, Sep 2010.

- [11] C Gutsche. First observation of electroweak z boson plus two jet production, October 2014.
- [12] M Capeans, G Darbo, K Einsweiler, M Elsing, T Flick, M Garcia-Sciveres, C Gemme, H Pernegger, O Rohne, and R Vuillermet. ATLAS Insertable B-Layer Technical Design Report. Technical Report CERN-LHCC-2010-013. ATLAS-TDR-19, Sep 2010.
- [13] C Gemme. The ATLAS Insertable B-Layer (IBL) Project. Jul 2011.
- [14] Claude Leroy and Pier-Giorgio Rancoita. *Principles of Radiation Interaction in Matter and Detection*. World Scientific, 2016.
- [15] Katherine Pachal. Search for new physics in the dijet invariant mass spectrum at 8 TeV, Jan 2015. Presented 01 Jun 2015.
- [16] Michele Livan and Richard Wigmans. Misconceptions about Calorimetry. *Instruments*, 1(1):3, 2017.
- [17] Lene Bryngemark, Torsten AKESSON, Else LYTKEN, and Johan RATHSMAN. Search for new phenomena in dijet angular distributions at  $s = 8$  and 13 TeV, Feb 2016. Presented 18 Mar 2016.
- [18] J.J. Goodson. *Search for Supersymmetry in States with Large Missing Transverse Momentum and Three Leptons including a Z-Boson*. PhD thesis, Stony Brook University, May 2012. Presented 17 Apr 2012.
- [19] Georges Aad et al. Technical Design Report for the Phase-I Upgrade of the ATLAS TDAQ System. Technical Report CERN-LHCC-2013-018. ATLAS-TDR-023, Sep 2013. Final version presented to December 2013 LHCC.
- [20] Morad Aaboud et al. Performance of the ATLAS Trigger System in 2015. *Eur. Phys. J.*, C77(5):317, 2017.
- [21] Yu Nakahama. The atlas trigger system: Ready for run-2. *Journal of Physics: Conference Series*, 664(8):082037, 2015.
- [22] M. Aaboud et al. Search for pair production of higgs bosons in the  $b\bar{b}b\bar{b}$  final state using proton-proton collisions at  $\sqrt{s} = 13$  TeV with the atlas detector. *Phys. Rev. D*, 94:052002, Sep 2016.



- [23] 2015 start-up trigger menu and initial performance assessment of the ATLAS trigger using Run-2 data. Technical Report ATL-DAQ-PUB-2016-001, CERN, Geneva, Mar 2016.
- [24] Simone Alioli, Paolo Nason, Carlo Oleari, and Emanuele Re. A general framework for implementing NLO calculations in shower Monte Carlo programs: the POWHEG BOX. *JHEP*, 06:043, 2010.
- [25] Torbjorn Sjostrand, Stephen Mrenna, and Peter Z. Skands. PYTHIA 6.4 Physics and Manual. *JHEP*, 05:026, 2006.
- [26] J. Pumplin, D. R. Stump, J. Huston, H. L. Lai, Pavel M. Nadolsky, and W. K. Tung. New generation of parton distributions with uncertainties from global QCD analysis. *JHEP*, 07:012, 2002.
- [27] Peter Zeiler Skands. Tuning Monte Carlo Generators: The Perugia Tunes. *Phys. Rev. D*, 82:074018, 2010.
- [28] D. J. Lange. The EvtGen particle decay simulation package. *Nucl. Instrum. Meth. A*, 462:152, 2001.